Point vortex modelling of the wake dynamics behind asymmetric vortex generator arrays

D Baldacchino, C Ferreira, D Ragni, and G J W van Bussel

Delft University Wind Energy Research Institute, Faculty of Aerospace Engineering, Kluyverweg 1, 2629 HS Delft, The Netherlands.

E-mail: d.baldacchino@tudelft.nl

Abstract. In this work, we present a simple inviscid point vortex model to study the dynamics of asymmetric vortex rows, as might appear behind misaligned vortex generator vanes. Starting from the existing solution of the infinite vortex cascade, a numerical model of four base-vortices is chosen to represent two primary counter-rotating vortex pairs and their mirror plane images, introducing the vortex strength ratio as a free parameter. The resulting system of equations is also defined in terms of the vortex row separation and the qualitative features of the ensuing motion are mapped. A translating and orbiting regime are identified for different cascade separations. The latter occurs for all unequal strength vortex pairs. Thus, the motion is further classified by studying the cyclic behaviour of the orbiting regime and it is shown that for small mismatches in vortex strength, the orbiting length and time scales are sufficiently large as to appear, in the near wake, as translational (non-orbiting). However, for larger mismatches in vortex strength, the orbiting motion approaches the order of the starting height of the vortex. Comparisons between experimental data and the potential flow model show qualitative agreement whilst viscous effects account for the major discrepancies. Despite this, the model captures the orbital mode observed in the measurements and provides an impetus for considering the impact of these complex interactions on vortex generator designs.

1. Introduction and background

The action of vortices embedded in boundary layers is often exploited as a means of flow control for transition or separation delay using vortex generator (VG) devices [1]. For flows prone to separation, the use of vortices enhances momentum in the wall region, delaying or even preventing separation. Vortex generators are applied on wind turbine blades following significant design iterations, involving VG integration studies using computations and wind tunnel testing of airfoil sections with and without VGs. This is likely complemented by an assessment of blade-bound flow for positioning of the VGs. Blade root flows likely pose different inflow conditions to the VG arrays than the simplified scenarios on wing sections, but the extent to which such discrepancies are considered during the blade design phase is unclear. Evidence of the complex inflow is for instance found in Micallef et al. [2] and Herráez et al. [3], through observations of appreciable spanwise flows in blade root regions. In addition, installation of the VG arrays involves a deal of uncertainty, compounded by effects of yaw misalingment, wind shear and gusting which can lead to excursions from design conditions. One possible consequence is that the VG arrays will experience a skewed inflow, relative to the cascade axis. Assessing the impact of such inflow conditions for VG arrays is of prime importance for understanding flow control performance in more practical conditions and for improving the robustness of VG designs.


Content from this work may be used under the terms of the Creative Commons Attribution 3.0 licence. Any further distribution of this work must maintain attribution to the author(s) and the title of the work, journal citation and DOI.
Published under licence by IOP Publishing Ltd

A VG array designed to produce equal counter-rotating (CtR) vortices, and which is subjected to a skewed inflow, will instead result in an unequal or asymmetric vortex cascade, as shown in Figures 1 and 2. However, the behaviour and dynamics of asymmetric vortex arrays have scarcely been addressed in literature. On the other hand, single trailing edge vortices and vortex pairs in ground effect have received much more attention, often motivated by understanding the behaviour of aircraft wakes during take-off and landing, close to the ground. The appearance of weaker secondary structures as a result of this interaction is also a well-known phenomenon and is relevant to the present study. Harvey and Perry [4] demonstrated that primary vortex rebound in ground effect was due to the separation of the crossflow boundary layer, giving rise to a secondary vortex which in turn influenced the path of the primary. In this case, the strength of the secondary became comparable to that of the primary. In other cases, as reported in Dee and Nicholas [5], the secondary strength was weaker, resulting in a spiralling trajectory about the primary vortex. Harris and Williamson [6, 7] studied a counter-rotating pair in ground effect and also observe the appearance of weaker secondary structures which in turn exhibit secondary instabilities. Secondary vortices have also recently been observed behind vortex generator vanes within turbulent boundary layers, as in Velte et al. [8] for a single vane and Lögdberg et al. [9] for a VG pair. In the latter, the relative strength of the secondary and primary structures was seen to increase in the direction of the freestream. More recently Velte et al. [10] observed the formation of multiple secondary structures behind a single VG vane and a complex phase space of the vane angle and relative boundary height was mapped and associated with a particular vortex system. The formation of particular vortex wakes was found to correlate with the strength and ground proximity of the primary vortex. A strong interaction of all structures is expected; however, such complex wakes are not observed in symmetric vortex array configurations [11].

In other instances, unequal vortices arise as a result of direct generation. Pauley and Eaton [12] analysed an asymmetric vortex pair in a turbulent boundary layer produced with vanes of different height, achieving a strength ratio of 0.5. They observed accelerated diffusion and distortion of the weaker vortex as well as rapid convection about the stronger vortex structure. This also resulted in a faster decay of the weak vortex. Lögdberg et al. [9] investigated asymmetric vortex arrays in the context of separation control on bluff-body vehicles. Despite the substantial effect on the vortex paths, skewed inflow was found to affect the boundary layer shape factor only minimally. These observations are supported by near-wake measurements of a VG array in Baldacchino et al. [13]. In the latter, spanwise planes up to 50 device heights downstream of a VG array were measured using stereo Particle Image Velocimetry (PIV) on a zero-pressure gradient, flat plate turbulent boundary layer. Asymmetry was created by rotating each individual VG pair of height $h = 5mm$ ($h/\delta = 0.25$) in an attempt to mimic the effects of skewed inflow. For a particular skew angle φ, suppressed vortex ejection was observed. In particular, an orbiting (or spiralling) motion is observed for the weak vortex, whilst maintaining its position in close proximity to the wall. This appears to correspond with the slightly lower (and hence farther from separation) shape factor which was measured for the same flow. This behaviour has not explicitly been observed previously. Indeed, the role inviscid vortex dynamics plays in the interaction of asymmetric vortex arrays within a boundary layer has not been addressed.

Early vortex generator designs were based optimisations of the vortex trajectories. An important objective was to maximise the vortex residence time in the vicinity of the wall where its effect is most required. Using a potential flow model, Jones [14] provided the framework for this purpose. An analytical function was found describing the paths of equal counter-rotating vortices in an infinite cascade. Following these developments, Pearcey [15] derived optimal VG designs, based purely on the kinematic properties derived from Jones' model. Despite the assumption of potential flow, measured near-wake vortex trajectories compared well with theory. However, vorticity diffusion and circulation decay posed modelling limitations. Vortex re-organisation in the boundary layer far downstream appears to explain lateral deviations from inviscid theory. Lögdberg et al. [9] modified Jones' model to account for these limitations and the resulting model captured better the actual

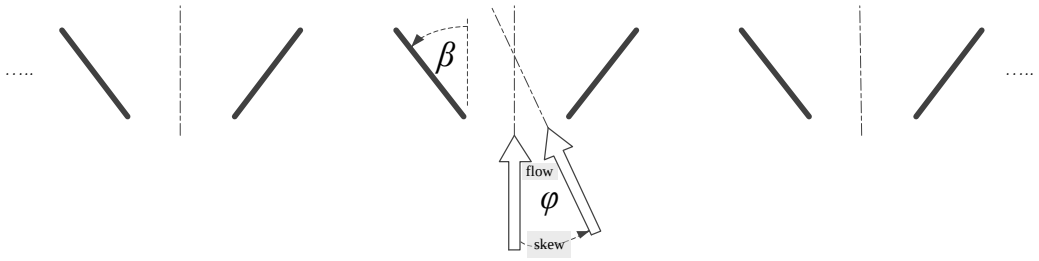

Figure 1: Expected influence of skewed inflow relative to a VG cascade

symmetric vortex dynamics in the far wake. Other computational efforts based on Computational Fluid Dynamics (CFD) have shown reasonable success in predicting vortex paths and the effect on the boundary layer (see for e.g. [16, 17]). However, aside from the added computational effort of CFD, a vortex modelling approach follows naturally for this flow problem, and can provide a useful physical interpretation of the complex vortex interactions.

Point vortex models have been used extensively throughout literature. Aref [18] details the potential of these simple models in modelling physical vortex systems. Von Kárman devised the $N = 2$ vortex model to describe the behaviour of the vortex-street and further derived stability criteria for this system [19]. More recently, Harris and Williamson [7] used a periodic point vortex model (PPVM) to study the dynamics of secondary vortices arising from the wall-interaction of a CtR vortex pair. Their model revealed different flow modes and showed consistent qualitative agreement with observations. Asymmetric trailing wakes from periodically oscillation bodies [20, 21] have also been tackled using PPVMs. For instance, Stremler et al. [20] found that translating or orbiting regimes can be expected depending on the initial spatial conditions and impulse of the system. Laminar staggered [22] and symmetrical bluff-body wakes were investigated in great detail by Basu [23]. These wakes are analysed using Hamiltonian dynamics and a detailed picture of the complex types of motion emerges. Agreement with experimental data is generally quite fair for this and other similar efforts in literature, but more important, considering the significant model assumptions and limitations, is the ability of these simple PPVMs to unravel governing dynamic mechanisms in wakes and other vortex dominated flows.

In the present case, we develop a PPVM to study the influence of unequal vortex strengths on cascades which are typically arranged for flow control purposes. In doing so, it is necessary to classify the range of possible motions and place them into a practical context. In contrast to the majority of previously documented efforts, the implementation allows for independently defined vortex strengths, in order to investigate the influence of the strength ratio on the resulting system dynamics. Experimental data on this particular flow is restricted, and PIV measurements for two cases could be used for validation of the new vortex model [13]. Ultimately, the goal of this paper is then to verify and validate the developed model and discuss the possible implications for practical flow control design.

2. Point Vortex Model

The wake flow induced by the cascade visualised in Figure 1 is numerically modelled by a system of asymmetric vortices using a periodic four-vortex system. This system contains the primary vortices (A,B) and their images (a,b), as depicted in Figure 2. The streamfunction $\psi(z, y)$ for a single periodic point vortex array as given in Saffman [24] is

$$\psi(z, y) = -\frac{\gamma}{4\pi} \ln \left[\cosh \kappa(y - y_0) - \cos \kappa(z - z_0) \right] \tag{1}$$

where γ is the vortex strength or circulation, (z, y) are the planar coordinates and $\kappa = {}^{2\pi}/_{D}$ defines a spatial frequency, or wave-number, of the infinite vortex cascade. The partial derivatives of (1) yields the velocities induced by a single point vortex cascade. Summing the contributions from all base vortices according to the system depicted in Figure 2, the dynamics of the i^{th} vortex (A or B) are given by

$$\begin{aligned} w_i(z,y) &= \frac{dz_i}{dt} = -\sum_{n=1}^{N}{}' \frac{\gamma_n}{2D} \cdot G_i^n(z,y) \\ v_i(z,y) &= \frac{dy_i}{dt} = \sum_{n=1}^{N}{}' \frac{\gamma_n}{2D} \cdot H_i^n(z,y) \end{aligned} \quad \text{where} \quad \begin{cases} G_i^n(z,y) = \left[\dfrac{\sinh \kappa(y_i - y_n)}{\cosh \kappa(y_i - y_n) - \cos \kappa(z_i - z_n)} \right] \\ H_i^n(z,y) = \left[\dfrac{\sin \kappa(z_i - z_n)}{\cosh \kappa(y_i - y_n) - \cos \kappa(z_i - z_n)} \right] \end{cases} \tag{2}$$

where the singular term for which $n = i$ is omitted, as indicated by the primed sum. Practically these describe the dynamics of N infinite vortex cascades, each with an internal spacing D. This is a well known general result (see e.g. Pozrikidis [19]), and as seen in the opening section has been applied to study different problems in fluid mechanics. Furthermore, to address the specifics of the problem, the vortex strength is retained in the sum as we wish to obtain a system parametrised by the relative strengths. For this purpose, Γ is introduced as the vortex strength ratio ${}^{\gamma_B}/_{\gamma_A}$, where we consider that $|\gamma_B| \leq |\gamma_A|$, without loss of generality. Here we draw a parallel to the recent work by Basu [23]. In the latter, the symmetrical, periodic, four-base vortex system chosen to represent the laminar bluff-body wake is mathematically equivalent to the present vortex model (see Figure 2). The bluff-body wake centreline corresponds to the ground plane in the present context and the implied symmetry reduces both systems to an identical $N = 2$ system. The present analysis proceeds in the context of VG wakes, as outlined in the opening section.

We continue to non-dimensionalise the kinematic equations by defining simple scaling quantities. Normalising the spatial coordinates (z, y) by the length scale ${}^{1}/_{\kappa}$, we obtain $\xi = \kappa z$, $\eta = \kappa y$. A time scale $\tau = D^2/(\pi\gamma_A)$ is also established, such that $T = {}^{t}/_{\tau}$. Substituting these definitions in (2), we obtain the form

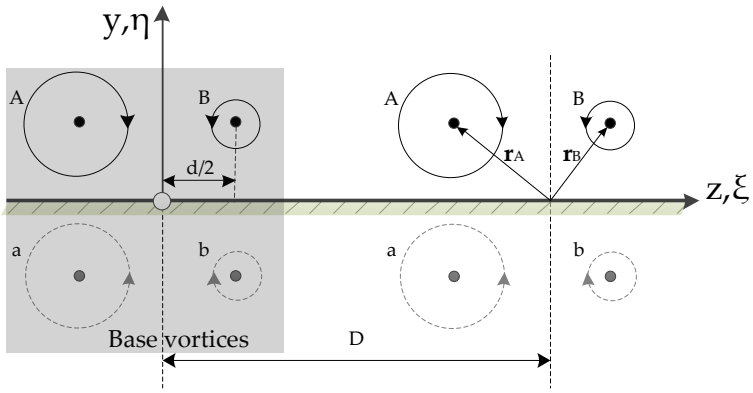

Figure 2: Conceptual vortex model with base vortices in shaded region and a periodic image shown with spacing D. Wall images are by definition constrained as $(x_a, y_a) = (x_A, -y_A)$ and $(x_b, y_b) = (x_B, -y_B)$, $\mathbf{r}_A$ and $\mathbf{r}_B$ being independently defined.

$$\left.\begin{aligned}\frac{d\xi_i}{dT} &= -\sum_{n=1}^{N}{}' \frac{\gamma_n}{\gamma_A}\cdot G_i^n(\xi,\eta)\\ \frac{d\eta_i}{dT} &= \sum_{n=1}^{N}{}' \frac{\gamma_n}{\gamma_A}\cdot H_i^n(\xi,\eta)\end{aligned}\right\} \quad \text{where} \quad \frac{\gamma_n}{\gamma_A}=\begin{cases}\pm\Gamma & \text{for } n=B,b\\ -1 & \text{for } n=a\end{cases} \tag{3}$$

where we note that, by definition, the mirror vortex strengths are simply $\gamma_a = -\gamma_A$ and $\gamma_b = -\gamma_B$. Trajectories are obtained through the time-integration of the velocity induced at each base-vortex location which is determined through equation (3). The system of ODEs is integrated in time using a fourth-order Runge Kutta scheme. Using a sufficiently small time step, a solution is obtained within a few seconds of computational time. Note that since we assume a decoupling of the 2D flow field from the out-of-plane flow, we can equivalently integrate spatially (in the out-of-plane coordinate, x) by considering some convective velocity U_c. This velocity can then be a prescribed constant, or more appropriately, the boundary layer velocity distribution might be considered along with the vortex core axial velocity [8].

3. Numerical Results

3.1. Model Verification

A simple verification step is presented to demonstrate correct implementation of the model. Recall that for the trivial case of equal strength and oppositely signed vortices ($\Gamma = -1$), Jones [14] found that the system dynamics reduce to an integrable (exact) ODE. Implementation of the present PPVM is therefore verified with this analytical result. The vortex paths projected in the z-y plane are given by the exact expression

$$cosec^2\xi + cosech^2\eta = K \tag{4}$$

where K is a conserved quantity determined by the initial vortex positions [14]. The numerical (3) and analytical (4) results are shown in agreement in Figure 3. From these graphs it is clear that for this configuration, vortices experience an initial wall-ward motion, followed by lateral displacement and ejection under the influence of the wall and adjacent pairs. The final approach is an asymptotic path away from the wall.

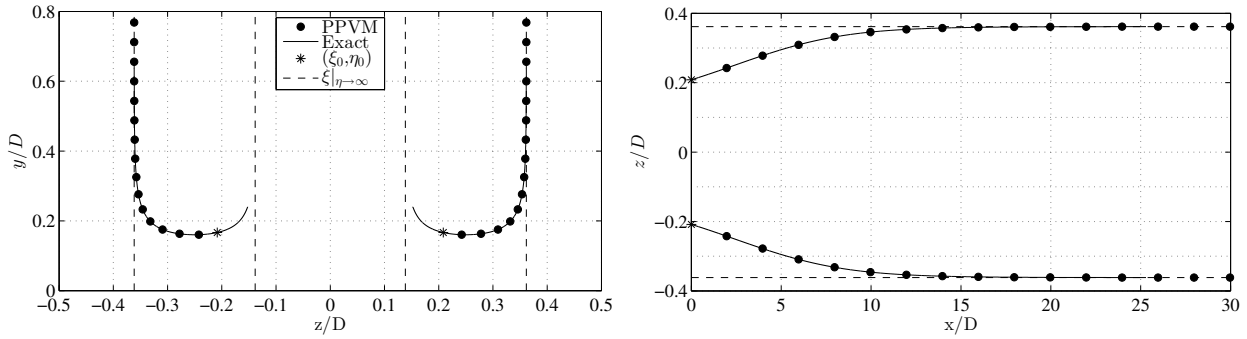

Figure 3: Verification of frontal (*left*) and planar (*right*) projected trajectories of the present PPVM with the analytical results (4). Single trajectory shown for $K = 1.71$, for $(\xi_0, \eta_0) = (\pm 5\pi/12, \pm\pi/3)$

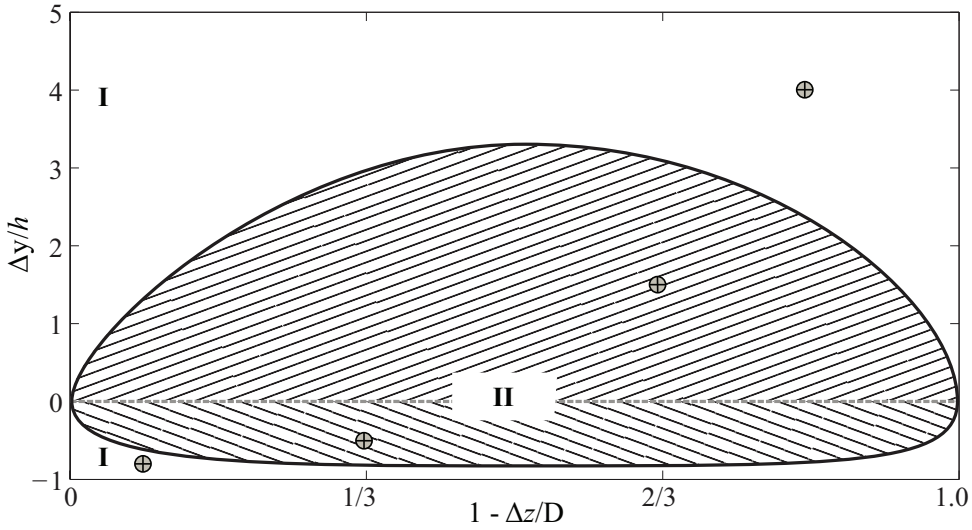

Figure 4: Regime diagram in $(\Delta z/D,\ \Delta y/h)$ space for $\Gamma = -1$. Area enclosed by heavy black contour indicates translating trajectories (Regime II). The orientation of hatched lines are only for indication of the general skew direction, which reverses on either side of the dashed grey line; the latter represents a vertical trajectory. Regime (I) outside the hatched area represents orbital trajectories. Example trajectories are sampled at the four indicated cross-hairs.

3.2. Influence of vortex row separation

The relative starting position of the vortex cascades essentially determines the ensuing motion. Thus for this part of the analysis, vortex trajectories were obtained through numerical integration of (3) for a total duration $\mathcal{T}$. Cases treated in this section pertain to $\Gamma = -1$. With a sufficiently discretised phase space, a regime diagram as shown in Figure 4 can be produced. Every point in this map is the result of a simulation conducted for a particular combination of $(\Delta z, \Delta y \mid \Gamma = -1)$. A contour is fitted to the discrete simulation values to produce this map after binning for the different classes of motion.

For oppositely signed and equal strength vortices, two regimes of motion emerge, each of which describes trajectories of qualitatively similar behaviour. These regimes are displayed in Figure 4. For intermediate spanwise spacings $\Delta z/D$, with small and large wall-normal separation $\Delta y/h$, vortex rows follow characteristically orbital motions. The initial positions giving rise to this motion are identified with Regime I. Sample trajectories for this motion are shown in Figures 5(a) and 5(d). The vortices trace cyclic paths, the properties of which are determined by the initial conditions. In these graphs, the base vortices are illustrated along with the mirror counterparts located on either side at $\pm D$ for illustrative purposes. Later on we will see that for all $-1 < \Gamma < 0$, the vortex rows describe orbital motion for all $(\Delta z, \Delta y)$.

The hatched area, Regime II, exists for intermediate values of $\Delta y/h$, for all $\Delta z/D$. This second regime represents a different type of motion in which vortex trajectories all follow a translating path, oriented according to the value of vertical displacement Δy. The resulting planar trajectories corresponding to operating points within this regime are illustrated in Figures 5(b) and 5(c). For the simple case of $\Delta y/h = 0$ (along the dashed grey line in Figure 4), the vortex rows essentially drive eachother away from the wall, normally, such that the row separation is bounded and becomes gradually constant. This essentially corresponds to the verification plots from Figure 3.

3.3. Influence of vortex strength ratio, Γ

In the previous section it was mentioned that any excursions from $\Gamma = -1$ result in an orbital type motion. Two combinations of $(\Delta z_0/D, \Delta y_0/h)$ previously sampled in the translating regime ((b)

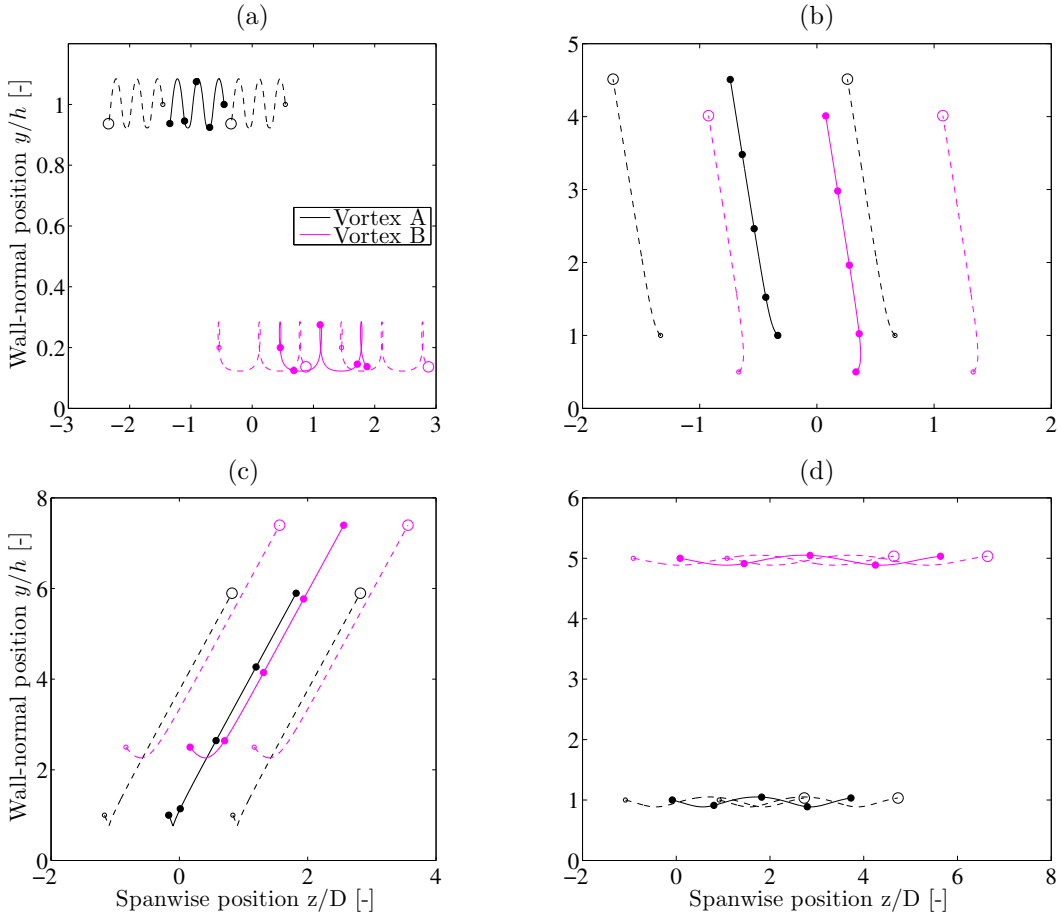

Figure 5: Trajectories for $\Gamma = -1$, for different initial conditions $(\Delta z_0/D, \Delta y_0/h)$: (a) 11/12,−0.8; (b) 2/3,−0.5; (c) 1/3,1.5 and (d) 1/6,4.0. Filled markers and solid lines represent the base vortices; empty markers and dashed lines represent their periodic images. Markers are spaced at $0.25\mathcal{T}$. Trajectories (a) and (b) are shown for a total time 1L/U, (c) for 5L/U and (d) 10L/U.

and (c) in Figure 5) are chosen to illustrate this fact. Trajectories for these initial conditions are shown for two values of Γ in Figure 6. All paths are now clearly cyclic in nature. As seen from Figures 5 and 6, we can expect a wide range of orbital behaviour. However, thus far, all orbiting trajectories have been grouped under one category. It is clear that further classification is possible by analysing the peak amplitude $\Delta y_{max}/2$ and cyclic frequency of the motion $\widetilde{t}$. Note that in contrast to the large majority of works in literature studying planar wakes evolving along the same plane (e.g. [20, 7, 22]), the present flow is an idealisation of a three-dimensional evolving flow. As a simplifying assumption, the in-plane vortex motions and the out-of-plane flow have been decoupled. Thus it may be useful to consider the 'orbiting' in this context as a general term encompassing helical or spiralling motions.

Two additional properties of the orbital trajectories are therefore established: (i) the normalised peak trajectory amplitude, $\mathcal{A} = \Delta y_{max}/2h$ and (ii) the normalised period of the orbital motion, $\mathcal{P} = \widetilde{t}/(L/U)$. These are illustrated in Figure 7 for the strong vortex with varying Γ. The plots in this figure were again obtained by a set of simulations for each $(\Delta z, \Delta y \mid \Gamma)$.

Thus far we have noted that any slight departure from exactly equal and opposite vortices, will also result in orbital motion. However from Figures 7, we notice how the maximum magnitudes of the amplitude and period decrease as $\Gamma \to 0$. The first case, $\Gamma = -0.9$ is chosen as a value close

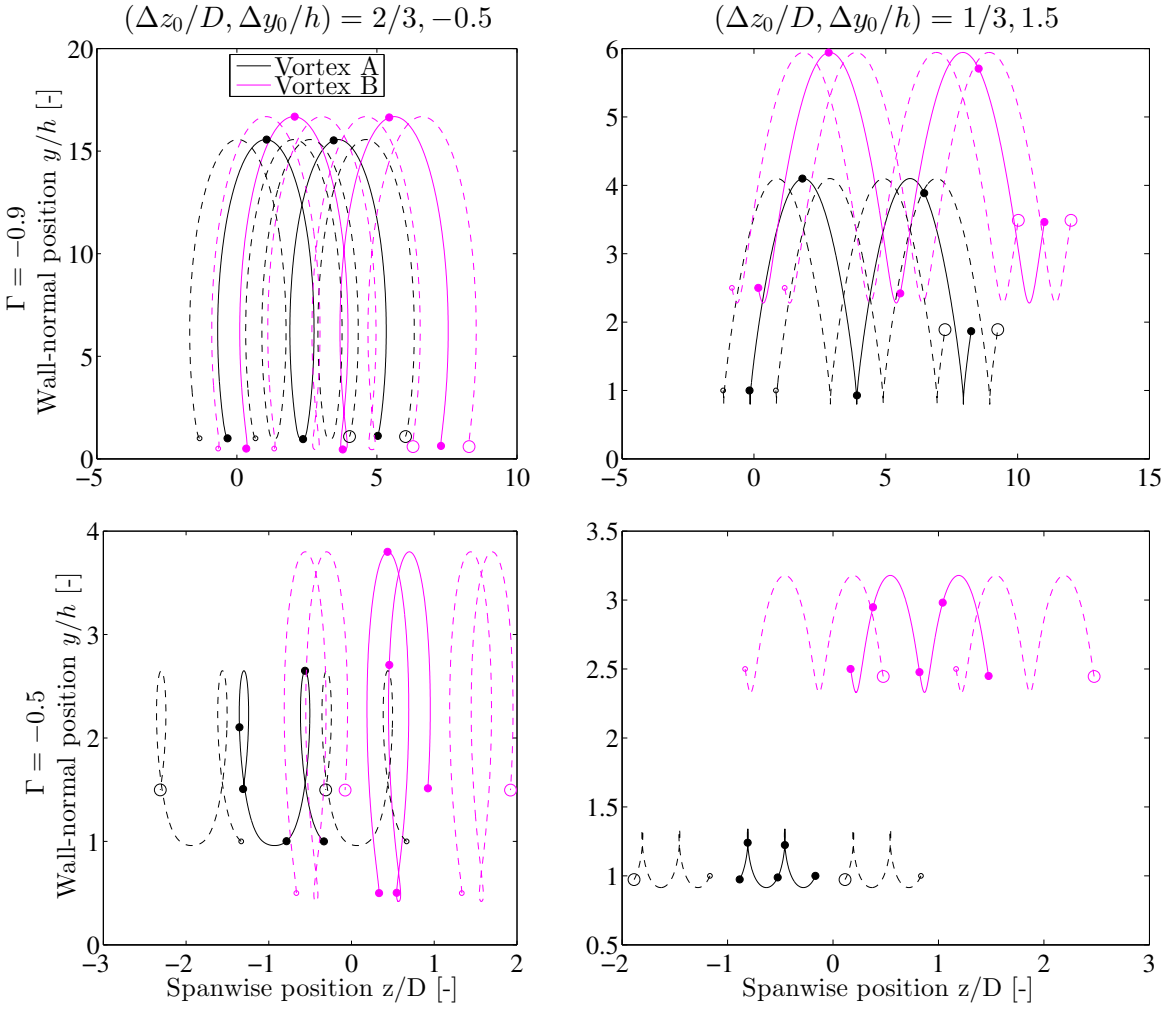

Figure 6: Trajectories for $\Gamma = -0.9$ (*top*) and $\Gamma = -0.5$ (*bottom*). Different initial conditions $(\Delta z_0/D, \Delta y_0/h)$ are prescribed: 2/3,−0.5 (*left*) and 1/3,1.5 (*right*). Filled markers and solid lines represent the base vortices; empty markers and dashed lines represent their periodic images. Markers are spaced at $0.25\mathcal{T}$. Trajectories for $\Gamma = -0.9$ and -0.5 are shown for a total time 20L/U and 5L/U.

to -1, as might for instance occur in VG experiments due to small unintended vane misalignments. Despite classification into an orbital trajectory, we notice how the amplitude is the largest of the three presented cases, and at least around 5 times the typical VG height, for intermediate $\Delta z/D$ and small $\Delta y/h$, the latter being representative of typical VG geometries. In the measurements of Lögdberg et al. [9], a wall-normal displacement of less than $1h$ at $400h$ downstream was observed. This slow ejection rate signifies that the amplitude scale predicted by the model, is far larger than that permitted in the real flow due to viscous effects. In any case, it would occur on a much longer length and time scale than that observed. For intermediate values of Γ, at -0.5 (middle panels, Figure 7), the amplitude scale decreases to the order of the initial vortex core radius (or vane height), and further still for $\Gamma = -0.1$. For $\Gamma = -1$ in Figure 4, orbital motion would only occur for impractically low or high values of $\Delta y/h$. However, the latest results of Figure 7 imply that with moderate Γ, orbital motion on the scale of the initial vortex wall-normal position becomes possible, and therefore, potentially relevant for practical applications.

In Figure 8, the effect of Γ is elucidated for two different initial positions, $(\Delta z_0/D, \Delta y_0/h) =$

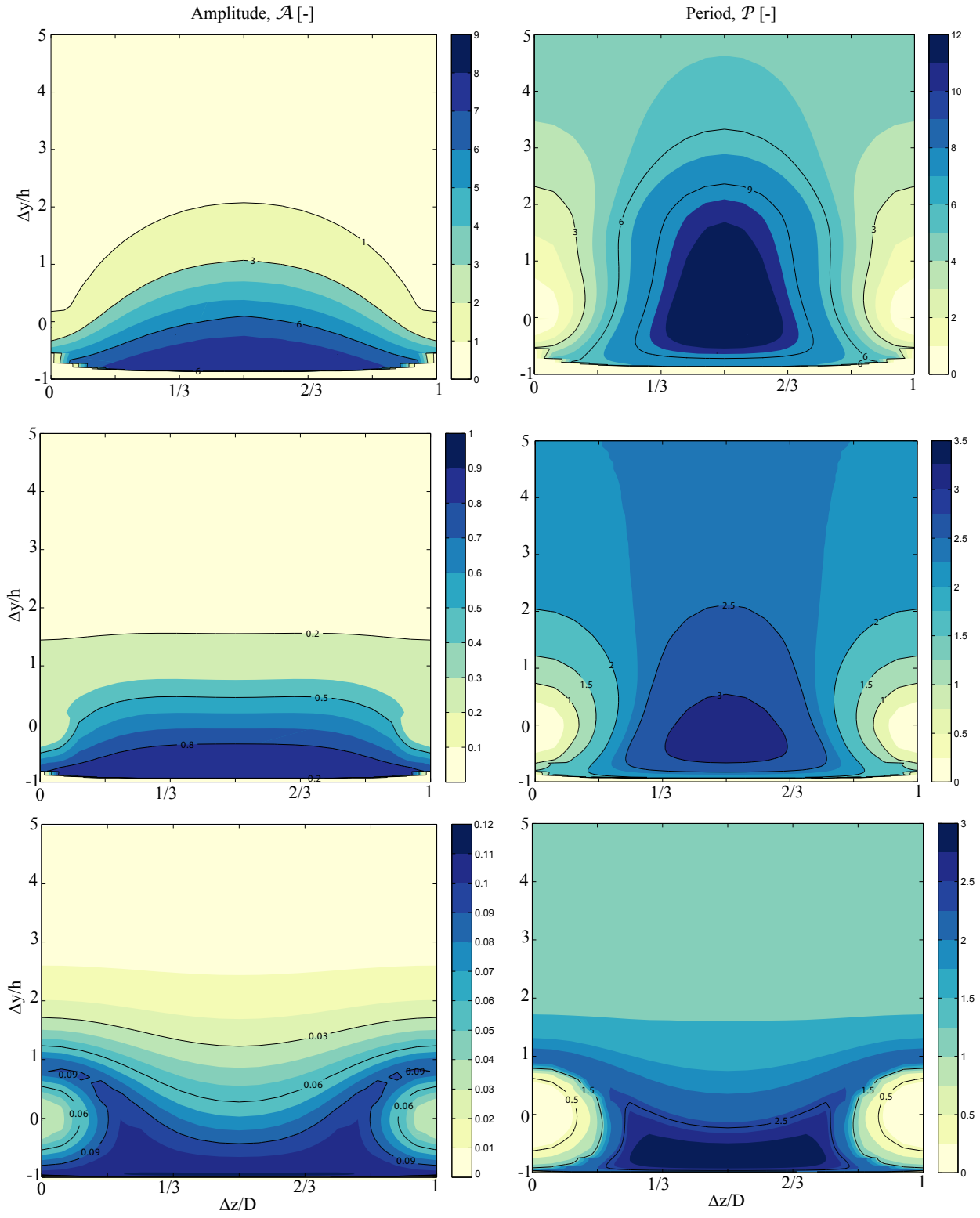

Figure 7: Amplitude (*left*) and period (*right*) of orbiting trajectories of the strong vortex for different values of Γ: (*top*) −0.9; (*mid*) −0.5; (*bottom*) −0.1.

(1/3,1.5) and (1/6,4.0). These initial conditions respectively produced translating and orbiting trajectories for $\Gamma = -1$. This is noted in the trends as the amplitude and period become degenerate

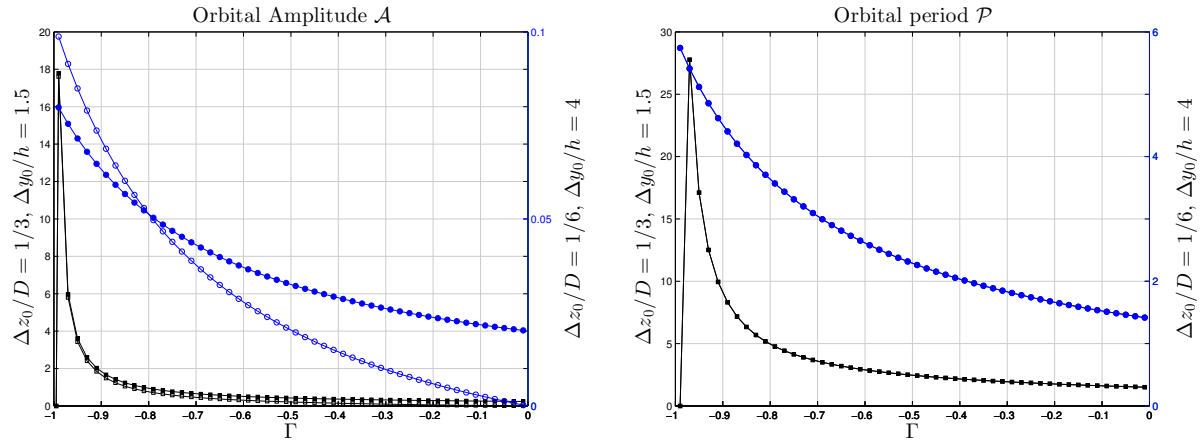

Figure 8: Influence of the vortex strength ratio on the orbital amplitude (*left*) and period (*right*) for the initial positions indicated on the ordinates. Solid and open symbols represent the weak and strong vorticies respectively.

(shown here as null) at $\Gamma = -1$ for the translating case, whereas the second sampled initial condition shows orbital behaviour (non-zero, finite $\mathcal{A}$ and $\mathcal{P}$). The characteristics of the strong and weak vortices are shown separately in Figure 8 and are clearly distinguishable. The weaker vortex row experiences a larger amplitude under the influence of the stronger vortex row for the initial condition (1/3,1.5). The second initial condition (1/6,4.0) shows a more complex behaviour as the relative amplitudes depends on Γ. Note also that as $\Gamma \to 0$, one vortex row becomes infinitely weaker than the other. This system would exhibit characteristics of a single co-rotating vortex row and is considered degenerate for the present study. It is therefore consistent that differences between the two vortices grow with decreasing $|\Gamma|$, in the absence of viscous dissipation. The trajectory period is identical for both vortices but determined by the initial conditions and strength ratio. These general observations are a direct consequence of the conservation of linear impulse for the vortex system.

4. Comparison with measurements

4.1. Results

PIV measurements from Baldacchino et al. [13] are used as a physical test case for the PPVM. Two cases are used from this study pertaining to a skewed inflow of $\varphi = 10°$ and 20°. Vanes in each VG pair are nominally oriented at $\beta = \pm 18°$; the skewed inflow effectively increases the angle on one vane, and reduces it on the other. Thus for $\varphi = 10°$, the vane angles become respectively 28° and −8°; for $\varphi = 20°$, vane angles are 38° and 2°, according to the convention defined in Figure 1. It is clear then how this sets up the case for the asymmetric vortex array. Flow field data from the $3h$ streamwise station was the closest to the VGs to yield reliable data. The vortex strength and core positions evaluated at this station were therefore used to initialise the simulations with the following boundary conditions: $(\Delta z_0/D, \Delta y_0/h \mid \Gamma) = (1/3, -1/10 \mid -1/3)$ for $\varphi = 10°$; $(\Delta z_0/D, \Delta y_0/h \mid \Gamma) = (0.30, -0.62 \mid -0.13)$ for $\varphi = 20°$. Note that in the experiments, $D = 30$ mm.

Results are first shown for $\varphi = 10°$ in Figure 9. The analytical streamfunction (1) is evaluated at the measured vortex positions at $10h$ downstream and compared with the experimental flowfield in the form of in-plane streamlines. Note that streamline spacing is the same for computations and measurements. Differences are immediately visible, most notably due to experimental limitations, such as near wall data availability, cross-flow and the fact that small misalignments in the VG placement result in slightly different initial vortex positions. This is also evident from differences at the side boundaries in Figure 9. Nonetheless, there is a good degree of qualitative similarities between the measured and modelled flow.

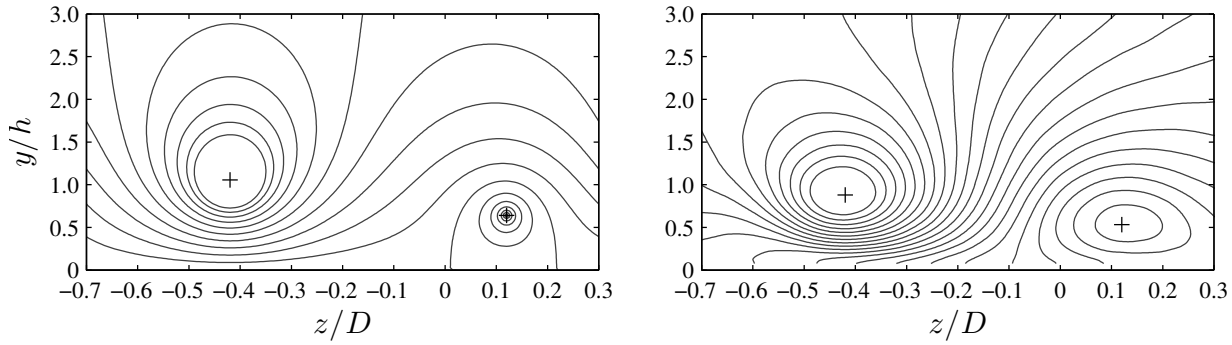

Figure 9: Streamfunction due to an unequal periodic array of point vortices, $\varphi = 10°$: (*left*) computed streamfunction, (*right*) 2D streamlines measured $10h$ downstream VG trailing edge; crosses represent vortex centres.

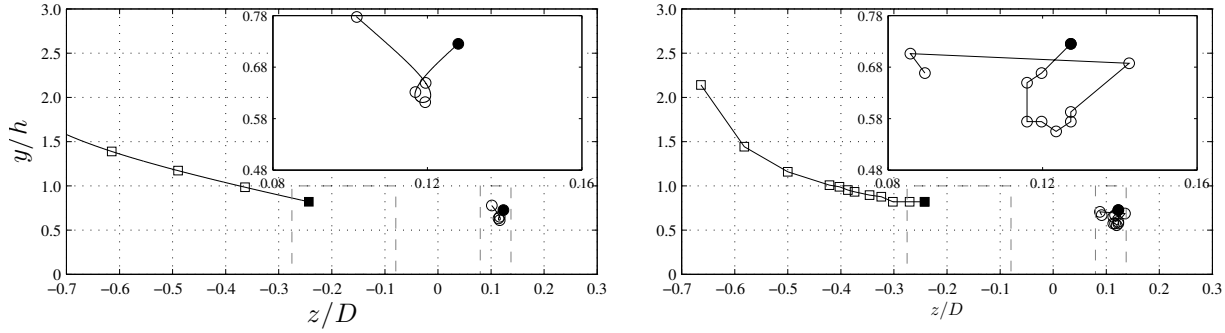

Figure 10: Primary base-vortex trajectories, $\varphi = 10°$: (*left*) computed paths, (*right*) measured paths; inserts show details of the weak vortex path; filled markers indicate initial vortex positions; dashed-grey contours represent the projected VG surface.

For the present case, path asymmetry arises not only due to the unequal strength of the vortices. The centre of the weak vortex lies consistently below the stronger vortex in the measurements. As we have seen, the array dynamics are highly sensitive to offsets in wall-normal separation, in addition to the strength ratio Γ. Referring to the orbital characteristics of Figure 7, we confirm that these starting conditions predict an orbital amplitude of around $0.5h$. The period appears higher than the actual length scale of the experiment and occurs due to the fact that we disregard the boundary layer velocity profile and axial velocity associated with the vortex. Both these would impose a smaller convective speed and thus the time scale would be higher. However, remarkably, the experimental and predicted regime of motions appear in agreement. The trend in the strong vortex path shows good overall agreement but the model predicts a slower ejection rate, as shown in Figure 10. This is likely due to the diffusion and growth of the vortex core, which is effectively manifested as a weak wall-normal motion. Similar observations are made for the case of $\varphi = 20°$ in Figures 11 and 12. The weak vortex is practically non-existent, in comparison with the stronger vortex, whose path is also slightly under predicted due to the presence of viscous effects.

4.2. Discussion

Despite the qualitative flow agreement between the inviscid vortex model and the measured core trajectories, the observations should be interpreted with some prudence. We therefore contrast these observations with the measurements of embedded streamwise vortices of Lögdberg et al. [9] and offer some interpretations on a possible connection. In the latter study, measurements indicated

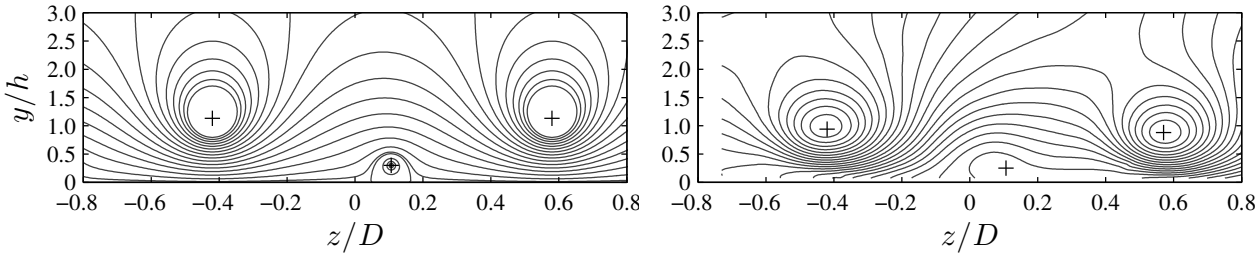

Figure 11: Same as Figure 9 for $\varphi = 20°$.

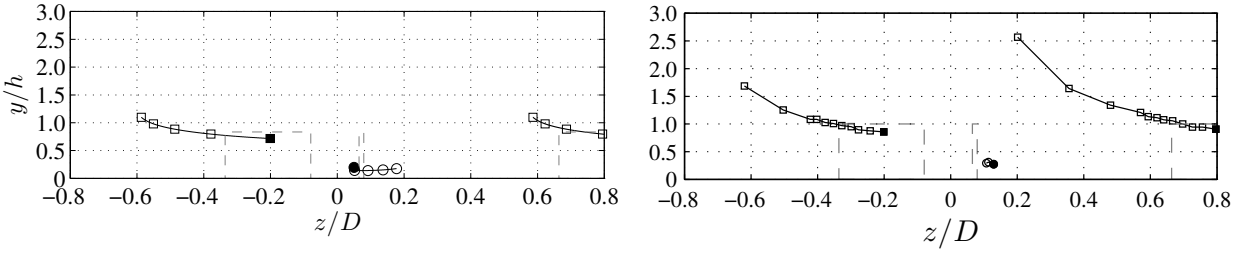

Figure 12: Same as Figure 10 for $\varphi = 20°$.

a lateral rebound, or "hook-like" motion of the vortices in the far region, becoming noticeable only after $50h$ for a symmetric VG array. The authors attributed this lateral inversion to the growth of the vortices in the boundary layer, which forces the vortices away from their inviscid trajectories to accommodate within the boundary layer. In the present case, the weak vortex undergoes a complete orbit within the $50h$ measurement region, comparable with model predictions, and much earlier than that reported in the case of Lögdberg et al. [9], suggesting a different mechanism. A key difference is of course the asymmetry in the present case, and one expects therefore that the stronger vortices grow at a faster rate than their weaker counterparts. This would give rise to a more prominent diffusion-driven lateral motion of the weak vortex, manifesting closer to the near wake of the VGs. It is therefore conceivable that the inviscid vortex dynamics and viscous-driven drifts constructively combine to give the orbital trajectory that has been observed.

Of course, the PPVM carries a number of simplifications which will limit practical applicability. Vortices are represented as singularities whose strengths implicitly remain constant in time in the absence of viscous dissipation. Spatial periodicity is imposed through the use of the infinite cascade solution (1), thus preventing intra-row interaction. Cross-flows have also been disregarded in this study. Throughout this paper, it is implied that asymmetric vortices result from off-design conditions and other non-idealities originating from the external flow. However, vortex breakdown can also lead to complex interactions. In practice, adverse streamwise pressure gradients can cause atypical transitional behaviour of the vortex core, a form of vortex breakdown [25]. In fact, this was recently evidenced as an intermediate core growth stage in Velte et al. [11]. The associated peak vorticity would also change, as would the vortex dynamics. Such transitional behaviour cannot be accounted for in the present model, and would likely invalidate predictions. The appearance of additional secondary structures is expected to influence the array dynamics but unless explicitly introduced, are outside the capabilities of the PPVM because viscosity is disregarded.

5. Concluding remarks

As a first step towards understanding the implications of off-design conditions on VG arrays, the complex blade flow has been simplified and modelled using the point vortex model with considerations of skewed inflow. The results presented have yielded useful insights into the dynamics of asymmetric vortex arrays. A review of literature showed very limited consideration of the dynamics of such wakes, more so within the context of VG arrays for separation control. To this end we have drawn novel parallels to recent analytical work of periodic, symmetric four-vortex systems in laminar bluff-body wakes [23]. The present work commenced with an exploration of the $(\Delta z, \Delta y, \Gamma)$ space, exposing translating and orbital regimes. The latter ensues for all unequal strength vortices. However, the predicted length and time scales for large $|\Gamma|$ are far larger than the initial vortex positions. Thus experimentally measured wakes, even in the absence of viscous effects (or high Reynolds numbers) are unlikely to reveal these cyclic motions. For intermediate values of Γ though, these scales rapidly decrease to the order of the initial vortex positions. This has in fact been validated with observations of orbital motion in an experimentally measured VG array wake.

From the perspective of VG design robustness, the uncertainty in vane misalignment is probably on the order of a few degrees, which means that a realistic range of Γ is probably much closer to unity. Thus some of the cases considered here are more likely worst case scenarios. Furthermore, the model requires further validation and the role of viscous diffusion requires a more consistent treatment. Nonetheless, through this analysis we have demonstrated that more complex vortex interactions may arise in practice, and may need to be considered for effective VG design.

Acknowledgements

This work is supported by the European Union's FP7 AVATAR project, conducted under the grant agreement No. FP7-ENERGY-2013-1/no. 608396.

References

[1] Lin J C 2002 *Review of research on low-profile vortex generators to control boundary-layer separation* vol 38
[2] Micallef D, Ferreira C, Sant T and van Bussel G 2014 *Wind Energy* **17** 657–669
[3] Herráez I, Akay B, van Bussel G J W, Peinke J and Stoevesandt B 2016 *Wind Energy Science* **2016** 1–33
[4] Harvey J K and Perry F J 1971 *AIAA Journal* **9** 1659–1660 ISSN 0001-1452
[5] Dee F S and Nicholas O P 1968 Flight Measurement of Wing Tip Vortex Motion near the Ground Tech. rep. CP 1065, British Aeronautical Research Council, London, England.
[6] Harris D M, Miller V A and Williamson C H K 2010 *Physics of Fluids* **22** 2–3 ISSN 10706631
[7] Harris D M and Williamson C H K 2012 *Journal of Fluid Mechanics* **700** 148–186 ISSN 0022-1120
[8] Velte C M, Hansen M O L and Okulov V L 2008 *Journal of Fluid Mechanics* **619** 167 ISSN 0022-1120
[9] Lögdberg O, Fransson J H M and Alfredsson P H 2009 *Journal of Fluid Mechanics* **623** 27 ISSN 0022-1120
[10] Velte C M, Hansen M O L and Okulov V L 2016 *Experimental Thermal and Fluid Science* **72** 31–39 ISSN 08941777
[11] Velte C M, Okulov V L and Hansen M O L 2011 *Physics of Fluids* **23** 1–4 ISSN 10706631
[12] Pauley W R and Eaton J K 1988 *AIAA* **26** 816–823
[13] Baldacchino D, Ragni D, Ferreira C and van Bussel G AIAA SciTech 2016-1259, USA *34th Wind Energy Symposium*
[14] Jones J P 1957 The Calculation of the Paths of Vortices from a System of Vortex Generators, and a Comparison with Experiment Tech. rep. A.R.C. Technical Report
[15] H H Pearcey 1961 *Boundary layer and flow control* ed Lachmann G V
[16] Fernández-Gámiz U, Zamorano G and Zulueta E 2014 *Journal of Physics: Conference Series* **524** 012024
[17] Spalart P R, Shur M L, Strelets M K and Travin A K 2015 *Flow, Turbulence and Combustion* ISSN 1386-6184
[18] Aref H 2007 *Journal of Mathematical Physics* **48** ISSN 00222488
[19] Pozrikidis C 2009 *Fluid Dynamics: Theory, Computation & numerical simulations* (Springer) pp 639–641
[20] Stremler M A, Salmanzadeh A, Basu S and Williamson C H K 2011 *Journal of Fluids and Structures* **27** 774–783 ISSN 08899746
[21] Xuzhao H and Gursul I 2016 *54th AIAA Aerospace Sciences Meeting* 1–26
[22] Basu S and Stremler M A 2015 *Physics of Fluids* **27** ISSN 10897666
[23] Basu S 2014 *Dynamics of vortices in complex wakes: modeling, analysis, and experiments* Ph.D. thesis Virginia Polytechnic Institute and State University
[24] Saffman P 1992 *Vortex Dynamics* (Cambridge) pp 130–133
[25] Escudier M 1988 *Progress in Aerospace Sciences* **25** 189–229 ISSN 03760421